

On the response of Martian ionosphere to the passage of a corotating interaction region: MAVEN observations

C. Krishnaprasad¹, Smitha V. Thampi¹, and Anil Bhardwaj²

¹Space Physics Laboratory, Vikram Sarabhai Space Centre, Thiruvananthapuram 695022, India

²Physical Research Laboratory, Ahmedabad 380009, India

Key Points:

- First direct comparison of the response of dayside and nightside ionosphere of Mars to the impact of a corotating interaction region (CIR)
- Observations of enhanced flux of precipitating suprathermal (>25 eV) heavy ions in the Martian exosphere during CIR period
- Indication of enhanced pickup ion induced depletion of nightside ionosphere during CIR event

arXiv:1908.00815v1 [physics.space-ph] 2 Aug 2019

Corresponding author: C. Krishnaprasad, kpchirakkil@gmail.com

Abstract

The response of Martian ionosphere to the passage of Corotating Interaction Region (CIR) of June 2015 is studied using observations from several instruments aboard the Mars Atmosphere and Volatile Evolution (MAVEN) mission. An intense CIR arrived at Mars on 22 June 2015, during which the upstream solar wind and interplanetary conditions were monitored by the Solar Wind Ion Analyzer, Solar Wind Electron Analyzer, Magnetometer, and Solar Energetic Particle instruments aboard MAVEN. The CIR event was characterized by enhancements in solar wind density, velocity, and dynamic pressure, and increased & fluctuating interplanetary magnetic field, and was accompanied by enhanced fluxes of solar energetic particles. The Langmuir Probe and Waves (LPW) instrument onboard MAVEN provided the ionospheric observations such as electron density and electron temperature during this period. The dayside ionosphere is significantly compressed only near the peak of solar wind dynamic pressure enhancement (~ 14 nPa). In contrast, on the nightside, the electron density remains depleted for a longer period of time. The electron temperatures are also enhanced during the period of electron depletion on the nightside. The STATIC (Suprathermal and Thermal Ion Composition) measurements show enhanced fluxes of suprathermal heavy ions in the Martian exosphere during CIR period, and evidences for enhanced tailward flow of these pickup ions. The analysis suggests that the nightside ionosphere is primarily controlled by the precipitating solar energetic particles and pickup ions transported across the Martian terminator, and depletes significantly when the heavy ion flux in the exosphere enhances.

1 Introduction

The interaction of solar wind with Mars is different from that of Earth. This is primarily because of the absence of an intrinsic global dipolar magnetic field on Mars [Russell, 1979; Acuña *et al.*, 1998, 1999]. A shock boundary defines the bow shock, where the solar wind changes from supersonic to subsonic speeds. The magnetosheath is a region of shocked, turbulent solar wind plasma behind the bow shock [Lundin *et al.*, 1991; Dubinin *et al.*, 1997]. The induced magnetospheric boundary or magnetic pileup boundary formed from the interplanetary magnetic field (through induced currents) is another plasma boundary within the magnetosheath, where the induced magnetosphere divert a significant fraction of solar wind plasma from further penetration into the Martian upper atmosphere. Hence, magnetic pileup region is a transition region from solar wind plasma to planetary plasma [Lillis *et al.*, 2015]. Another plasma boundary called ionopause defines the altitude where the solar wind dynamic pressure balances the ionospheric pressure [Duru *et al.*, 2009; Vogt *et al.*, 2015]. The topside ionosphere of Mars is mainly controlled from top by solar wind interaction [Vogt *et al.*, 2015]. The presence of remnant crustal magnetic fields (strongest in the southern hemisphere) makes the interaction picture more complex [Arkani-Hamed and Boutin, 2004; Acuña *et al.*, 1998; Connerney *et al.*, 2005, 2015; Lillis *et al.*, 2015].

The spatial variability in the coronal expansion and solar rotation cause solar wind flows of different speeds to become radially aligned. Compressive interaction regions are formed when a high-speed solar wind runs into slower plasma ahead. These compression regions (bounded by the forward and reverse shocks) form spirals in the solar equatorial plane that corotate with the Sun. Because the pattern of compression rotates with the Sun when the outflow pattern from the Sun is time-stationary, these high pressure regions are known as corotating interaction regions, or CIRs [Parker, 1958; Sarabhai, 1963; Carovillano and Siscoe, 1969; Smith and Wolfe, 1976; Gosling and Pizzo, 1999]. The high-speed streams (HSS) in CIRs are associated with coronal holes, which recur for more than one solar rotation. The track of interplanetary traveling CIRs from Sun through the interplanetary space to large heliospheric distances were previously studied by Williams *et al.* [2011] and Priše *et al.* [2015], with observations from spacecrafts en-route and in orbit around different solar system objects. The effect of CIRs on terrestrial ionosphere have been extensively

studied (e.g. *Borovsky and Denton [2006]*). But, a similar level of understanding is not achieved on our understanding of the impacts of CIRs on Mars and Venus because of the dearth of observations especially due to the lack of simultaneous solar wind and magnetic field monitors near the space environment of these planets.

Interplanetary coronal mass ejections (CMEs) and CIRs are the major solar wind dynamic pressure pulse events. These solar phenomena play a major role in space weather and ion escape at Mars [*Ma et al., 2014; Curry et al., 2015; Jakosky et al., 2015; Sánchez-Cano et al., 2017*]. Previously *Ma et al. [2017]* used a time-dependent global magnetohydrodynamic (MHD) model to investigate the response of the Martian ionosphere and induced magnetosphere to a large solar wind disturbance associated with the interplanetary CME on 8 March 2015. The MAVEN observations as well as model results showed that ion escape rates could be an order of magnitude enhanced in response to the high solar wind dynamic pressure during the CME event. *Luhmann et al. [2017]* used a data-validated MHD model to study the same event and an extreme CME event of July 2012. Their results also suggest enhanced solar wind pressure, magnetic field, and convection electric field combine to produce strong magnetospheric coupling with important consequences in ionosphere energization and escape.

Hara et al. [2011] (*Diéval et al. [2013]*) first reported enhancement (reduction) in the precipitation of heavy ions (solar wind protons and alpha particles) due to finite gyroradius effects. The upstream solar wind dynamic pressure and interplanetary magnetic field (IMF) are important factors in controlling the global spatial pattern and flux of ions precipitating into the Martian upper atmosphere, with intense ion precipitations when gyroradii of pickup ions (planetary ions accelerated by the motional solar wind convective electric field) are relatively small [*Hara et al., 2017*]. The study by *Martínez et al. [2019]* showed increase in precipitation ion flux by more than one order of magnitude during the arrival of September 2017 CME event compared to average flux during quiet solar wind conditions. Heavy pickup ion precipitation is the primary cause of atmospheric sputtering [*Leblanc et al., 2015, 2018; Wang et al., 2015; Chaufray et al., 2007*].

There are a few studies on the influence of CIRs and HSS on the Martian magnetosheath and ionosphere, primarily using data from plasma analyzers. For instance, *Dubin et al. [2009]* studied the impact of February 2008 ionospheric storm, induced by a corotating interaction region, on the Martian topside ionosphere, using observations from Analyzer of Space Plasma and Energetic Atoms (ASPERA-3) and Mars Advanced Radar for Subsurface and Ionospheric Sounding (MARSIS) onboard Mars Express (MEX) spacecraft. They have found that the clouds of dense and high pressure solar wind plasma penetrate the induced magnetospheric boundary to lower altitudes. These solar wind plasma clouds scavenge the topside ionospheric plasma, making the latter become rarefied and fragmentary. This causes energization of ions and an enhanced loss of volatiles from Mars (a factor of ≥ 10 enhancement in topside ionospheric erosion) [*Dubin et al., 2009*]. *Morgan et al. [2010]* have studied the CIR encounter with Mars on December 2015 using MARSIS/MEX radar sounding observations. They observed two radar absorption events separated by 26 days; and concluded that these surface reflection absorption events are caused by enhanced ionospheric ionization from high fluxes of energetic particles accelerated by the shocks associated with CIR. The Martian ionospheric variability during variable solar wind conditions, such as CIRs and CMEs were investigated by *Oppenorth et al. [2013]*. The solar wind conditions were obtained from proxy measurements at 1 AU. The study reports magnetosphere and ionosphere compression during solar wind dynamic pressure variations, and signatures of increased plasma transport over the terminator and enhanced ion outflow from the upper atmosphere [*Oppenorth et al., 2013; Sánchez-Cano et al., 2017*].

A characteristic heavy-ion signature was observed with ASPERA-3/MEX in the vicinity of Martian ionosphere during the passage of a CIR in September to October 2007 [Hara *et al.*, 2011]. Wei *et al.* [2012] have observed enhanced escape flux of oxygen ions in the Martian magnetosphere using observations from ASPERA-3/MEX. They have also compared the O^+ escape from polar region of Earth with that of MEX observations for the same CIR event, and concluded that same level of increase in upwelling oxygen ions was observed on Earth’s poles in comparison with Mars. The solar wind dynamic pressure enhancements was more affecting the ion escape on Mars, while dipole field effectively prevents such coupling of solar wind kinetic energy to planetary ions in the case of Earth [Wei *et al.*, 2012]. Elliott *et al.* [2013] have found that Martian magnetosheath electron fluxes are enhanced during the CIRs and HSS. They also concluded that the electron flux in the ionosphere of Mars does not respond to the CIRs and HSS, although the average electron energy is enhanced, as observed in the electron spectrometer in ASPERA-3/MEX. Harada *et al.* [2017] reported irregular structures in the topside Martian ionosphere following a CIR-related interplanetary shock using MARSIS/MEX and upstream MAVEN observations.

From the above discussion, it is clear that we need to improve further our understanding on the impact of CIRs on the Martian plasma environment, especially the ionosphere and the exosphere. Corotating solar wind streams of June 2015 provide a unique opportunity to study the response of Martian ionosphere to the CIR streams, using the suite of in-situ particles and fields observations from Mars Atmosphere and Volatile EvolutioN (MAVEN [Jakosky *et al.*, 2015]) spacecraft. This event is also unique as this is one of the largest CIR event, in terms of the solar wind dynamic pressure and density, ever observed at Mars and one of the highest recorded by MAVEN [Lee *et al.*, 2017]. We use observations from Langmuir Probe and Waves (LPW [Andersson *et al.*, 2015]) instrument to show the electron density as well as electron temperature measurements made by MAVEN during the period of study. We also use observations from Solar Wind Ion Analyzer (SWIA [Halekas *et al.*, 2015]), Magnetometer (MAG [Connerney *et al.*, 2015]), and Solar Energetic Particle (SEP [Larson *et al.*, 2015]) instruments to show the upstream solar wind, energetic particle, and magnetic field conditions, and Suprathermal and Thermal Ion Composition (STATIC [McFadden *et al.*, 2015]) instrument observations for the mass resolved ion energy flux information in the lower energy range compared to SEP. The solar wind electron and ionospheric photoelectron energy flux observations from Solar Wind Electron Analyzer (SWEA [Mitchell *et al.*, 2016]) are also obtained during this period. Together, this is a unique and comprehensive dataset, covering a wide energy range, which can help to gain new insights into the impact of CIRs on Martian space weather.

2 Data and Method of Analysis

The upstream solar wind parameters (density, dynamic pressure, and velocity) and IMF are computed from the SWIA onboard moments and MAG measurements (intensity and direction of the magnetic field) following the method by Halekas *et al.* [2016]. The SEP fluxes are obtained from the SEP instrument. The Level 2, Version 01, Revision 01 (V01_R01) data of SWIA, Level 2, Version 01, Revision 02 (V01_R02) data of MAG, and Level 2, Version 04, Revision 02 (V04_R02) data of SEP are used for upstream solar wind observations. The Level 2, Version 01, Revision 01 (V01_R01) onboard survey spectral data from SWIA and Level 2, Version 04, Revision 01 (V04_R01) survey spectral data from SWEA are used.

The LPW instrument provides observations of electron density (n_e), electron temperature (T_e), and electric field waves in the ionosphere of Mars [Ergun *et al.*, 2015; Fowler *et al.*, 2015; Andrews *et al.*, 2015]. There are two Langmuir probes, mounted on 7.1 m length booms, onboard MAVEN. It works in both LP mode and waves mode. The electron density and temperature in the LP mode are derived from the current–voltage (I–V) characteristics [Andersson *et al.*, 2015]. To understand the average quiet time picture of

the ionospheric electron density profiles, the average of 6 orbits in the similar solar zenith angle (SZA) regime, prior to the CIR arrival are used. The LP mode electron temperature Level 2, Version 03, Revision 02 (V03.R02) data and waves mode electron density Level 2, Version 02, Revision 02 (V02.R02) data are used for analysis. The Level 2, Version 02, Revision 00 (V02.R00) ion energy flux (data product C0), and mass resolved ion energy flux (data product C6) from STATIC instrument are used for observations of energy spectrum of protons and heavy ions in the Martian ionosphere and exosphere [Steckiewicz *et al.*, 2015]. STATIC is an energy, mass, and angular ion spectrometer (consisting of a toroidal “top hat” electrostatic analyzer with a $360^\circ \times 90^\circ$ field-of-view, combined with a time-of-flight (TOF) velocity analyzer with 22.5° resolution in the detection plane) that can record ion fluxes, with a base time resolution of 4 seconds, as a function of energy (0.1 eV - 30 keV), mass (1 - 70 amu), azimuth direction (0 - 360°), and deflection angle ($\sim \pm 45^\circ$) [McFadden *et al.*, 2015]. The MAVEN datasets shown in this paper are latest available and are downloaded from the Planetary Data System (<https://pds.nasa.gov/>).

SWIA measures the energy and angular distributions of solar wind and magnetosheath ions of energy between 25 eV to 25 keV in 48 energy steps. SWEA measures the energy and angular distributions of solar wind and magnetosheath electrons and ionospheric photoelectrons of energy between 3 eV and 4600 eV in 64 energy steps. SEP measures the energy spectrum and angular distribution of solar energetic ions of energy between 20 keV to 6 MeV in 28 energy steps and solar energetic electrons of energy between 20 keV to 1 MeV in 15 energy steps. STATIC measures the velocity distributions and mass composition of suprathermal and thermal ions in the energy range 0.1 eV to 30 keV and in the mass range 1 amu to 70 amu (64 energy bins and 2 mass bins in the data product C0, 32 energy bins and 64 mass bins in the data product C6) [Jakosky *et al.*, 2015]. The Wang-Sheeley-Arge (WSA)–ENLIL+Cone model simulations during June 2015 are taken from <http://helioweather.net/>, <https://iswa.ccmc.gsfc.nasa.gov/>. In this global heliospheric model, the solar coronal model WSA is coupled with the three-dimensional MHD numerical model ENLIL [Odstrcil, 2003], which is combined with the Cone model, so as to numerically simulate the interplanetary solar wind plasma and magnetic field conditions and to provide a global heliospheric context. The National Solar Observatory Global Oscillation Network Group (GONG) synoptic magnetograms are used as input for model runs (see Mays *et al.* [2015] and references therein for a detailed description of WSA–ENLIL+Cone model).

3 Observations

The Solar Dynamic Observatory Atmospheric Imaging Assembly (SDO/AIA) composite images of the Earth-facing disk of the solar corona during May through July 2015 indicate the presence of persistent mid- to low-latitude coronal holes for several solar rotations [Lee *et al.*, 2017]. The images of coronal hole in May, June, and July are shown in Figure 7 of Lee *et al.* [2017]. The CIR associated with the coronal hole triggered a moderate geomagnetic storm on 7 June 2015, and a minor geomagnetic storm on 4 July 2015 at Earth [Lee *et al.*, 2017]. The coronal hole rotated towards Mars, and the SWIA solar wind observations indicate the arrival of a CIR at Mars on 22 June 2015. The WSA–ENLIL+Cone simulations confirms that the same coronal hole with negative IMF polarity is rotated towards Mars and the stream arrive at Mars on 22 June 2015 (not illustrated, see Lee *et al.* [2017], Figure 4d). Figure 1a–1d shows the solar wind density, dynamic pressure, velocity, and IMF ($|B|$, B_x , B_y , and B_z) conditions during 16 to 24 June 2015. After a period of ~ 26 days (that is, one solar rotation period), on 17 July 2015, the CIR recurred at Mars, but the event was weaker (~ 1 nPa enhancement in solar wind dynamic pressure) in comparison with the first one [Lee *et al.*, 2017] and therefore no significant effects were observed on the ionosphere. In this study, we present the observations only for the June 2015 event.

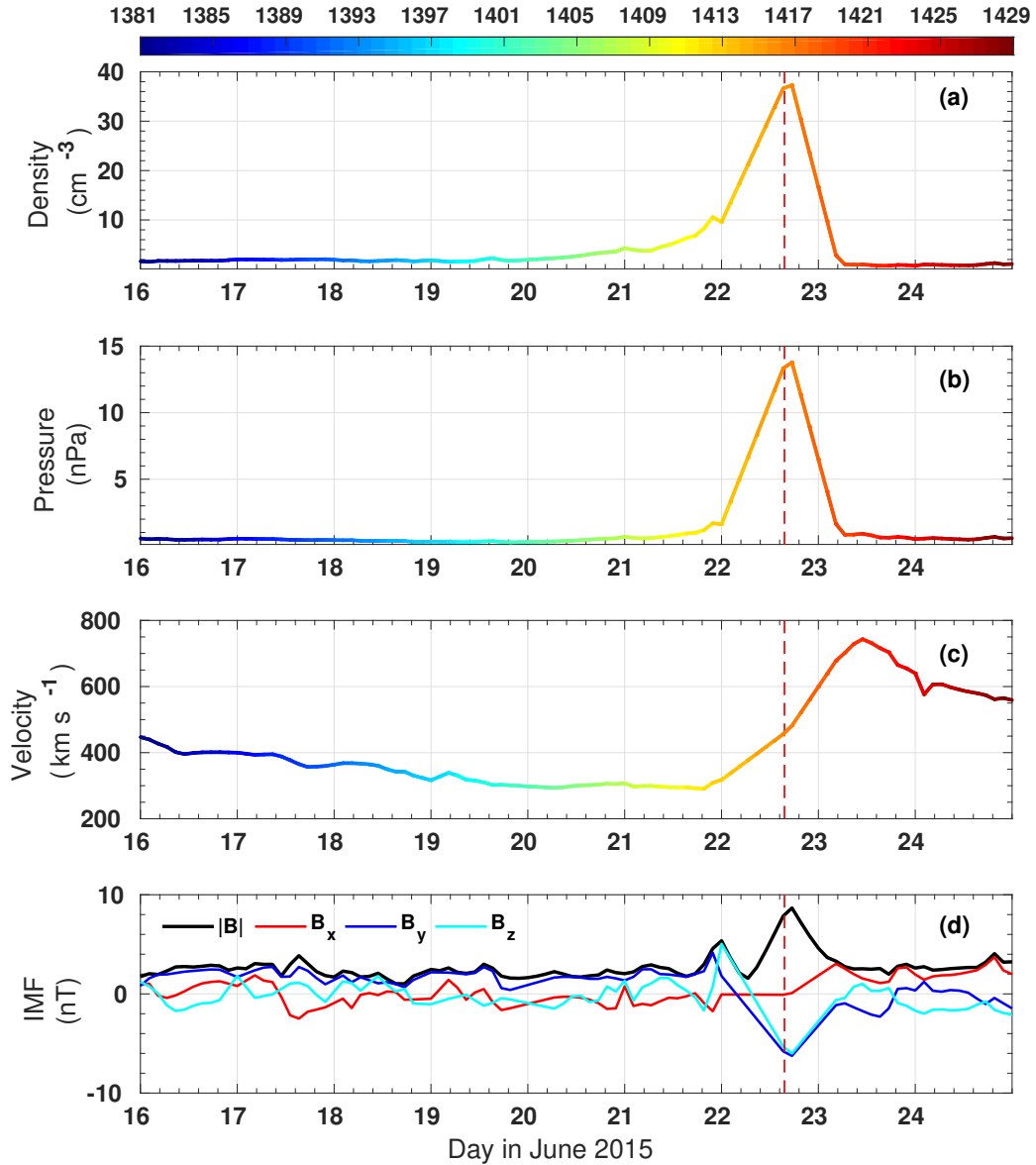


Figure 1. The upstream solar wind and interplanetary magnetic field conditions during June 2015 observed by SWIA: (a) solar wind density, (b) solar wind dynamic pressure, (c) solar wind velocity, and MAG: (d) IMF ($|B|$, B_x , B_y , and B_z). The color bar shows the orbits during the period. The periaapsis of orbit 1416 inbound/1417 outbound is marked with red dashed line on the graph.

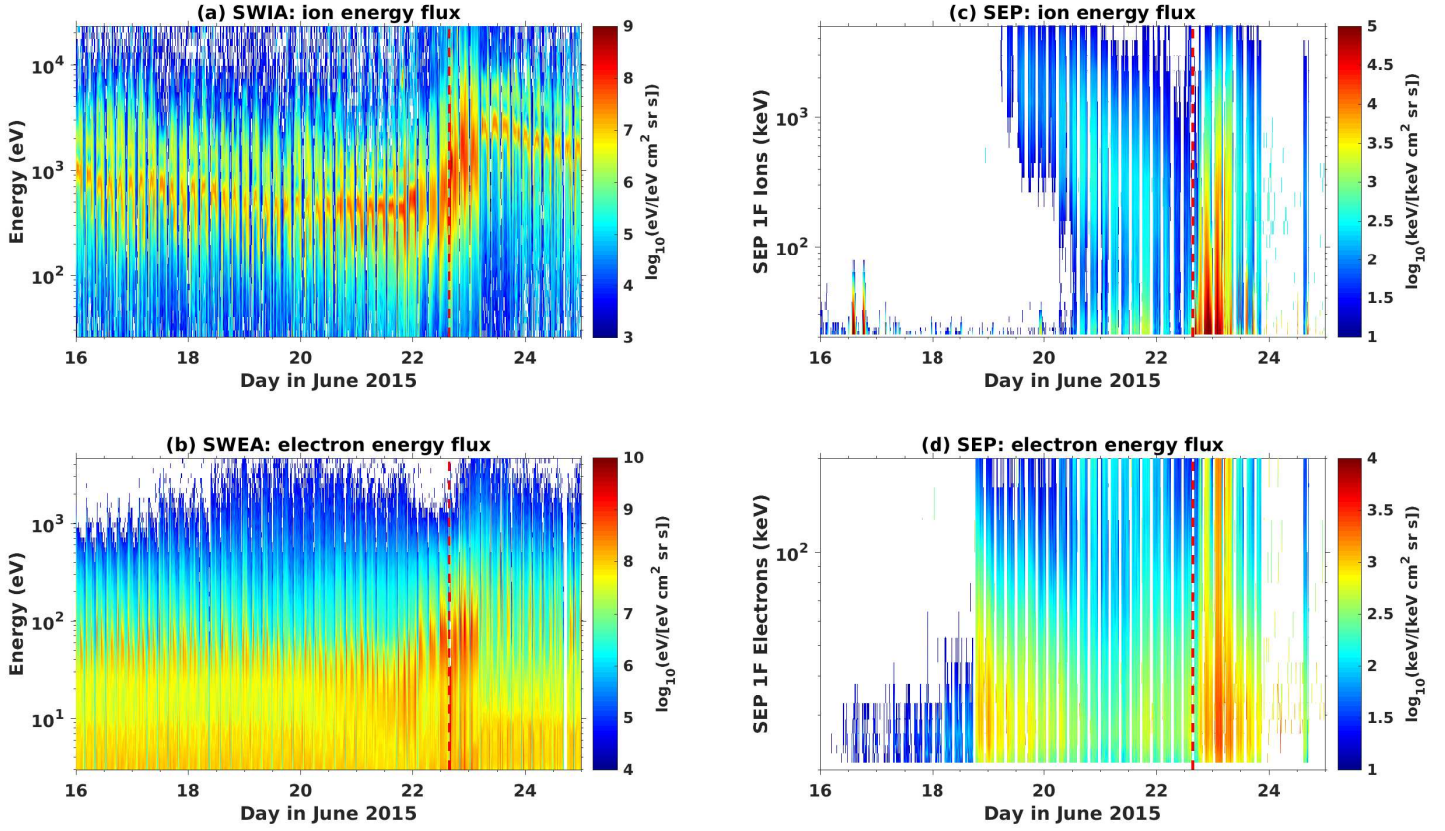


Figure 2. (a) SWIA energy-time spectrogram of ion energy flux during 16 to 24 June 2015. (b) SWEA energy-time spectrogram of electron energy flux during 16 to 24 June 2015. (c) Differential energy flux of SEP 1F ions during 16 to 24 June 2015. (d) Differential energy flux of SEP 1F electrons during 16 to 24 June 2015. The periapsis of orbit 1416 inbound/1417 outbound is marked with red dashed line on each spectrum. The initial white gaps in (c, d) are when the energy flux is below $10 \text{ keV}/[\text{keV cm}^2 \text{ sr s}]$, while white gaps on and after 24 June is due to absence of good quality data.

Figure 1 shows the upstream solar wind and IMF conditions (in the right-handed Mars-Sun-Orbit [MSO] frame, with x-axis pointing toward the Sun and z-axis parallel to the normal to Mars’ orbital plane) during 16-24 June 2015. The peak enhancement in dynamic pressure was ~ 14 nPa, on 22 June 2015 with peak density of ~ 40 cm^{-3} , velocity of ~ 800 km sec^{-1} (which remains high, that is about >400 km sec^{-1} until the end of the month), and total IMF peaked at ~ 9 nT. Also the magnetic sector switches from $(-B_x, +B_y)$ to $(+B_x, -B_y)$, and B_z oscillates from positive to negative to positive (Figure 1d). *Lee et al.* [2017] observed that the IMF configuration fluctuated between Parker spiral configuration and radial configuration, upon crossing the heliospheric current sheet associated with the HSS. The peak enhancements in upstream solar wind parameters was observed on 22 June 2015, 16:45 UTC when the compression region (peak density, dynamic pressure, and magnetic field) arrived at ~ 1.5 AU. These observations indicate that the CIR event was one of the strongest observed stream interaction region event at Mars, since in most of the previously reported events the maximum solar wind dynamic pressure encountered was ~ 10 nPa [*Dubinin et al.*, 2009]. This is more than the peak dynamic pressure observed by MAVEN during the 8 March 2015 interplanetary CME event [*Thampi et al.*, 2018; *Lee et al.*, 2017]. The MAVEN orbit during the peak of CIR dynamic pressure enhancement was orbit 1416 (inbound)/1417 (outbound). (For the MAVEN data presented here, a new orbit number starts when the instrument is at the geometric periapsis, and is the same for the outbound and the next inbound sectors, and incremented at the next periapsis.)

Figure 2a shows the SWIA energy–time spectrogram of omnidirectional ion energy flux during 16 to 24 June 2015. The solar wind ion energy corresponding to the peak flux increased from ~ 500 eV (on 22 June 2015) to ~ 5000 eV (on 23 June 2015). The solar wind ion energy spectrum follows the solar wind velocity pattern (Figure 1c). The solar wind ion flux enhanced from $\sim 10^7$ to $> 10^8$ $\text{eV}/[\text{eV cm}^2 \text{ sr s}]$ (with ion energies > 3000 eV) during the arrival of compression region. Figure 2b shows the SWEA energy–time spectrogram of omnidirectional electron energy flux during 16 to 24 June 2015. An enhancement in energy of the peak flux (300 eV) and flux of electrons (from $\sim 10^8$ to $> 10^9$ $\text{eV}/[\text{eV cm}^2 \text{ sr s}]$) during 22-23 June 2015 is observed.

The CIR event was associated with enhanced solar energetic particle (SEP) fluxes, with the arrival of SEP ions from 22 June 2015, 18:00 UTC (Figure 2c) and SEP electrons from 21 June 2015, 14:00 UTC (Figure 2d). The SEP ion enhancement is studied in detail in comparison with the observations at 1 AU to understand the acceleration of particles associated with CIR events (*Thampi et al.* [2019], manuscript submitted to ApJL). The SEP electron flux increased from $\sim 10^2$ to $> 10^3$ $\text{keV}/[\text{keV cm}^2 \text{ sr s}]$ with a corresponding order of magnitude increase in energy. Similarly, SEP ion flux increased to more than 10^3 $\text{keV}/[\text{keV cm}^2 \text{ sr s}]$ in the higher energy channels. There is a significant enhancement in SEP electrons from 18 June, 19:00 UTC and SEP ions from 19 June, 15:00 UTC prior to the arrival of the shock associated with CIR. These may be the SEPs associated with a CME that erupted on 18 June at $\sim 17:10$ UTC, and are streamed along magnetic field lines towards Mars, even-though the CME shock did not hit Mars [*Lee et al.*, 2017].

Table 1 (Table 2) shows the LPW periapsis measurement altitudes, longitudes, latitudes, solar zenith angles (SZAs), and time in UTC, with day of June 2015 and orbit number, for representative quiet orbits, viz, 1381, 1382, 1384, 1385, and 1386 and disturbed orbits, viz, 1415 (1416), 1416 (1417), 1417 (1418), 1418 (1419), 1419 (1420), and 1420 (1421) during inbound (outbound) leg of MAVEN. (As mentioned earlier, the convention followed here is that a new orbit number starts when MAVEN is at the periapsis, and is the same for the outbound and the next inbound sectors, and incremented at the next periapsis.) The SZA on the topside night time ionosphere are between 108° to 98° (inbound leg, altitude from 500 km to 200 km), while on the topside day time ionosphere are between 85° to 75° (outbound leg, altitude from 200 km to 500 km), for the disturbed period orbits.

Day/ Orbit #	UTC (hr)	UTC (hr)	Alt (km)	Alt (km)	Lon (deg)	Lon (deg)	Lat (deg)	Lat (deg)	SZA (deg)	SZA (deg)
INBOUND	From	To	From	To	From	To	From	To	From	To
16/1381	3.7	3.9	498.4	164.4	58.8	344.2	-74.3	-45.2	104.3	84.1
16/1382	8.2	8.4	498.9	164.9	124.5	49.5	-74.3	-45.3	104.5	84.4
16/1383	12.6	12.8	499.8	164	190.7	114.7	-74.3	-45.5	104.6	84.6
16/1384	17.1	17.3	499.6	164.8	256	180	-74.3	-45.7	104.7	84.8
16/1385	21.5	21.7	498.5	164.5	321.6	245.2	-74.2	-45.8	104.8	85.1
17/1386	2	2.2	498.4	163.7	27.4	310.4	-74.2	-45.9	104.9	85.3
22/1415	11	11.2	498.5	164.8	131.2	42.4	-73.3	-49.7	107.7	92
22/1416	15.4	15.6	498.9	163.9	197.2	107.7	-73.2	-49.8	107.8	92.2
22/1417	19.9	20.1	499.8	164.3	262.8	172.9	-73.1	-50	107.9	92.4
23/1418	0.3	0.5	498.9	164.3	328.3	238.2	-73.1	-50	107.9	92.6
23/1419	4.8	5	499.7	163.4	34.2	303.4	-73	-50.2	108	92.8
23/1420	9.2	9.4	499.6	164.5	99.6	8.7	-73	-50.3	108.1	93.1

Table 1. LPW measurement altitudes, longitudes, latitudes, SZAs, and time in UTC (with day of June 2015 and orbit number) for representative quiet orbits and disturbed orbits during inbound leg of MAVEN (measurement below 500 km altitude).

Figure 3a shows the nightside (near terminator) electron density profiles during 16 to 24 June 2015. Orbits 1415 to 1419 shows depletion in electron density compared to the mean quiet time profile. The mean quiet time profile with standard deviation is shown for comparison. The ionopause altitude observed for these two orbits are below 380 km. Also shown are two ‘normal’ profiles. Here orbit 1384 is a pre-CIR nominal profile, while orbit 1420 is a post-CIR profile which has returned to the normal quiet time behavior, and both are within the standard deviation of the mean quiet time profile, confirming that they show typical quiet time state.

Figure 3b shows the dayside (near terminator) electron density profiles during 16 to 24 June 2015. Orbits 1417 and 1418 shows deviation in electron density profile compared to the mean quiet time profile. Here orbit 1385 is a pre-CIR nominal profile, while orbit 1421 is a post-CIR profile, which has returned to the normal behavior. Here during orbit 1417, that is, the MAVEN orbit right during the peak of the solar wind dynamic pressure maximum, the electron density profile shows a lower ionopause (~ 400 km). But in contrast to the nightside, on the dayside the effects of CIR are observed in only one orbit, while on the nightside we observe the effect of CIR impact in five consecutive orbits. The orbit 1418 passes through the crustal field region and is seen to be structured compared to the previous orbit profile [Dong *et al.*, 2015].

If we compare the quiet time behavior during day and night, it is evident that the variability is less in the dayside. The higher standard deviations for the nightside profile indicate that the nightside ionosphere of Mars is more variable compared to the dayside which corroborates with the previous observations [Girazian *et al.*, 2017]. The profiles during the CIR event are significantly different from their representative quiet time mean profile and also well beyond the standard deviation, confirming that the deviations we discuss are

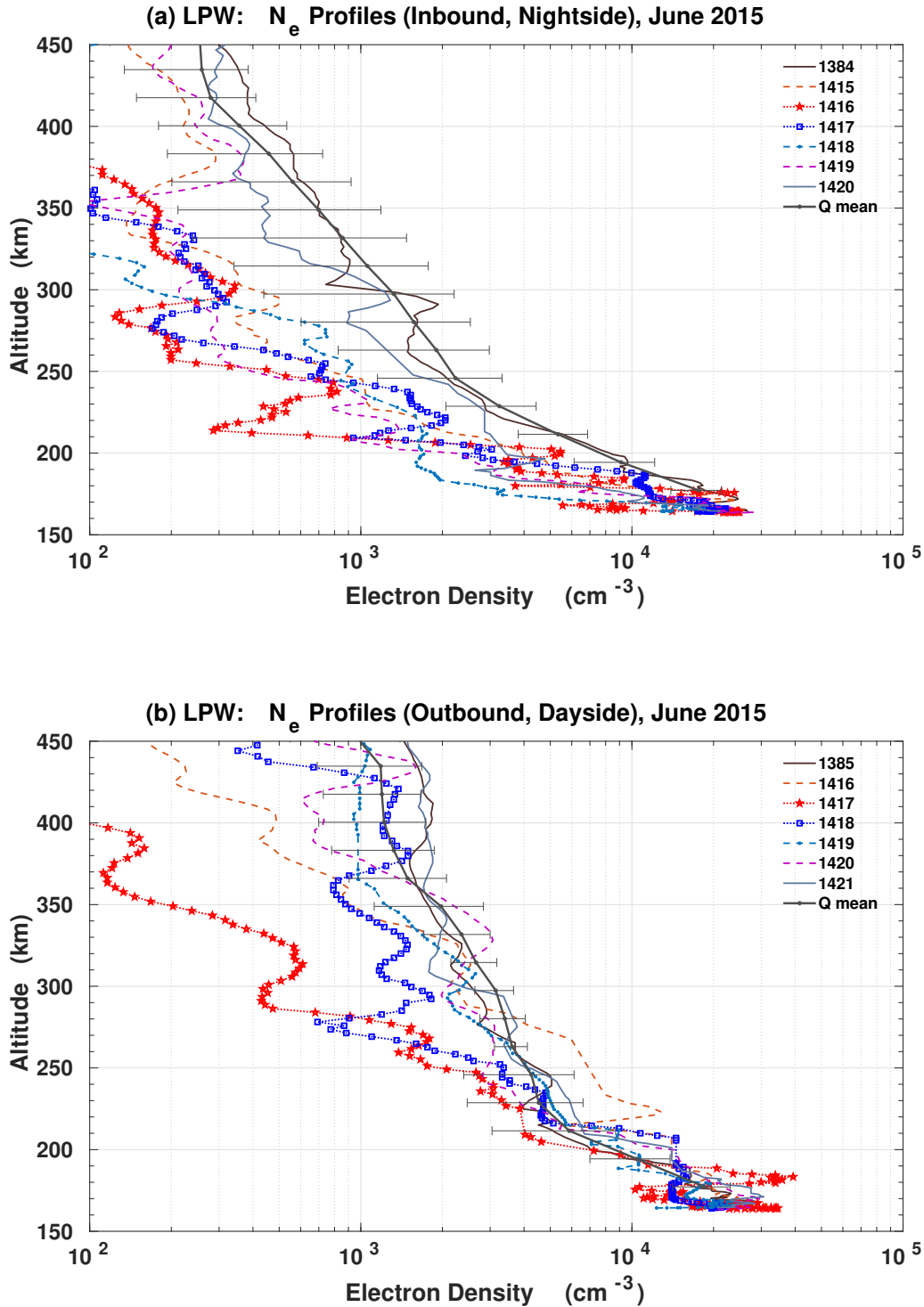


Figure 3. (a) The nightside electron density profiles during June 2015 observed by LPW. The orbits 1415, 1416, 1417, 1418, & 1419 are disturbed period orbits. Orbit 1384 is one of the pre-CIR quiet orbit and orbit 1420 is post-CIR quiet orbit. The black thick solid line with errorbar represents the mean quiet time profile and standard deviation of quiet orbits 1381, 1382, 1383, 1384, 1385, & 1386. (b) The dayside electron density profiles during June 2015 observed by LPW. The orbits 1416, 1417, 1418, 1419, & 1420 are disturbed period orbits. Orbit 1385 is one of the pre-CIR quiet orbit and orbit 1421 is post-CIR quiet orbit. The black thick solid line with errorbar represents the mean quiet time profile and standard deviation of quiet orbits 1381, 1382, 1383, 1384, 1385, & 1386.

Day/ Orbit #	UTC (hr)	UTC (hr)	Alt (km)	Alt (km)	Lon (deg)	Lon (deg)	Lat (deg)	Lat (deg)	SZA (deg)	SZA (deg)
OUTBOUND	From	To	From	To	From	To	From	To	From	To
15/1381	23.5	23.7	164	499.8	278.9	266.5	-44.9	-3.7	83.8	66.6
16/1382	3.9	4.1	164.4	499.6	344.2	331.7	-45.1	-3.8	84	66.9
16/1383	8.4	8.6	165	498.2	49.4	36.9	-45.2	-4.1	84.3	67.2
16/1384	12.8	13	164	499.2	114.7	102.1	-45.4	-4.1	84.5	67.4
16/1385	17.3	17.5	164.8	498.9	179.9	167.3	-45.5	-4.3	84.8	67.6
16/1386	21.7	21.9	164.5	499.2	245.2	232.5	-45.6	-4.4	85	67.9
22/1416	11.2	11.4	164.8	498.3	42.4	28.3	-49.6	-8.6	91.9	75.5
22/1417	15.6	15.8	163.9	499.9	107.6	93.5	-49.7	-8.6	92.1	75.7
22/1418	20.1	20.3	164.3	499.6	172.8	158.7	-49.8	-8.7	92.4	76
23/1419	0.5	0.7	164.3	498.6	238.1	223.9	-49.9	-8.9	92.6	76.3
23/1420	5	5.2	163.4	498.3	303.3	289.1	-50	-9	92.8	76.5
23/1421	9.4	9.6	164.5	499.9	8.6	354.3	-50.2	-9.2	93	76.7

Table 2. LPW measurement altitudes, longitudes, latitudes, SZAs, and time in UTC (with day of June 2015 and orbit number) for representative quiet orbits and disturbed orbits during outbound leg of MAVEN (measurement below 500 km altitude).

significant and are beyond the expected quiet time orbit-to-orbit variations, both for the dayside and for the nightside.

Figure 4a shows the nightside electron temperature profiles with SZA during 16 to 24 June 2015 (47 inbound orbits from 1381 to 1428). The electron temperature increases to ~ 14000 K during orbit 1416. The increase in temperature can be observed in the profiles obtained from the nightside legs of five consecutive inbound orbits from orbit 1415 to 1419. Figure 4b shows the dayside electron temperature profiles with SZA during 16 to 24 June 2015 (47 outbound orbits from 1382 to 1429). The electron temperature increases to ~ 11000 K during outbound of orbit 1417 on the dayside ionosphere.

Figures 5 to 7 shows the STATIC energy-time spectrogram and mass-time spectrogram of omnidirectional ion energy flux in C0 and C6 modes, respectively, during quiet (Figures 5a-5c) and disturbed (Figures 5d-5f, 6, 7) periods. The altitude and SZA during the MAVEN orbit legs corresponding to the STATIC observations are also shown. Figures 5a-5c shows the spectrogram during quiet time, before the arrival of CIR, and this corresponds to the periapsis of orbit inbound 1384/outbound 1385. We can see that there is no significant flux of heavy ions observed at higher altitudes. STATIC can measure suprathermal ions in the ionosphere and corona, and we can see a significant enhancement in flux of O^+ ($\text{amu}/q=16$) and O_2^+ ($\text{amu}/q=32$) ions as a consequence of the CIR arrival (Figures 5d-5f, 6, 7). We can also observe the enhanced flux of penetrating solar wind protons (H^+ , $\text{amu}/q=1$) into the ionospheric altitudes during CIR period (e.g. Figure 5b). The picked up heavy ions shown in the vicinity of Mars are of energies above 25 eV upto few keV (e.g. Figure 6a). The STATIC measured ion energy flux returns to the quiet time state afterwards (orbit number 1420/1421), with spectra very similar to that shown in Figures 5a-5c (not illustrated). This is in agreement with the LPW observations of electron density profiles on the nightside,

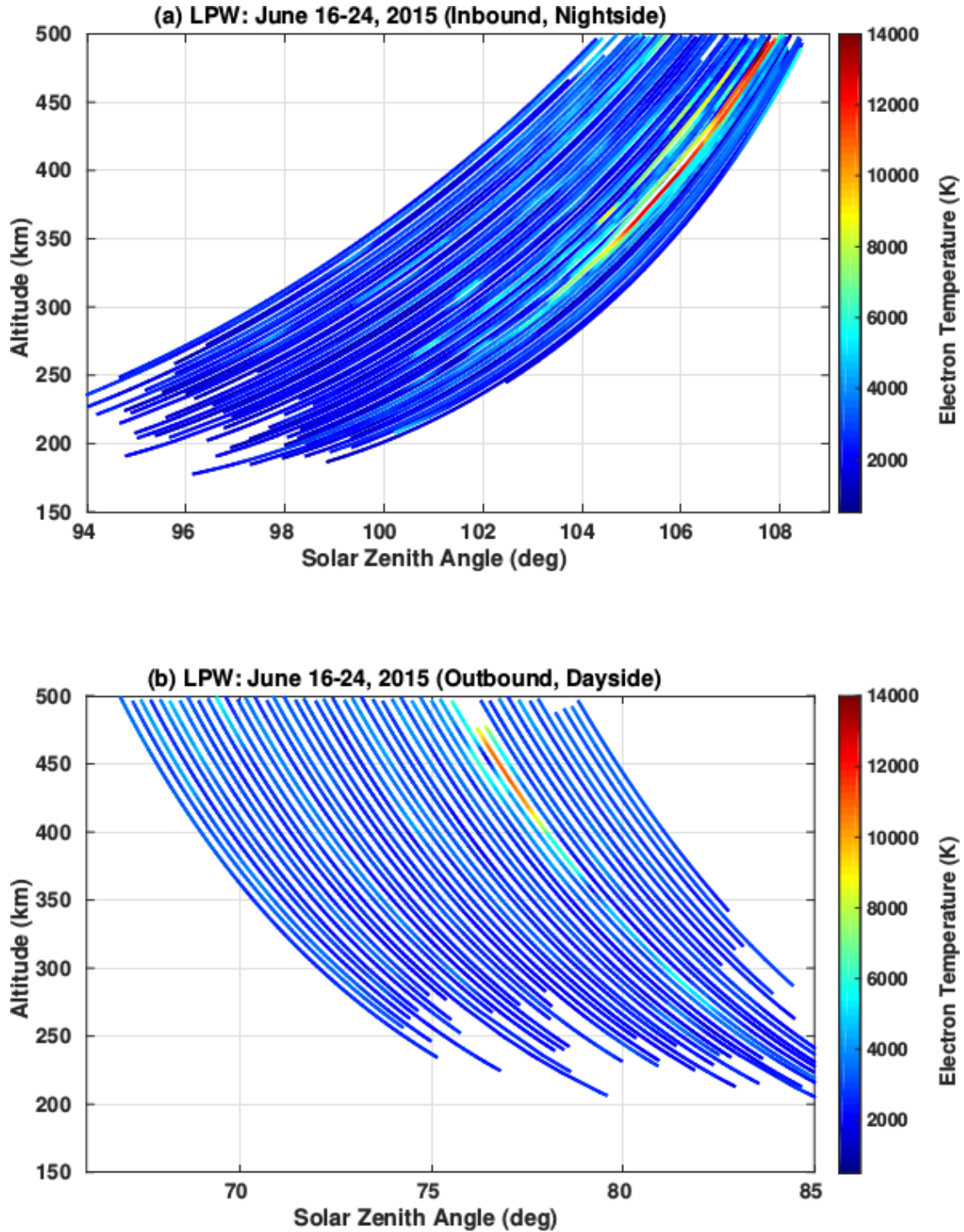


Figure 4. (a) The nightside electron temperature profiles with SZA during 16 to 24 June 2015 observed by LPW (Orbits 1381 to 1428 – from left to right). The nightside electron temperature is enhanced to more than 12000 K during inbound orbits 1416 and 1417. (b) The dayside electron temperature profiles with SZA during 16 to 24 June observed by LPW 2015 (Orbits 1382 to 1429 – from left to right). The dayside electron temperature is enhanced to more than 9000 K during outbound orbit 1417.

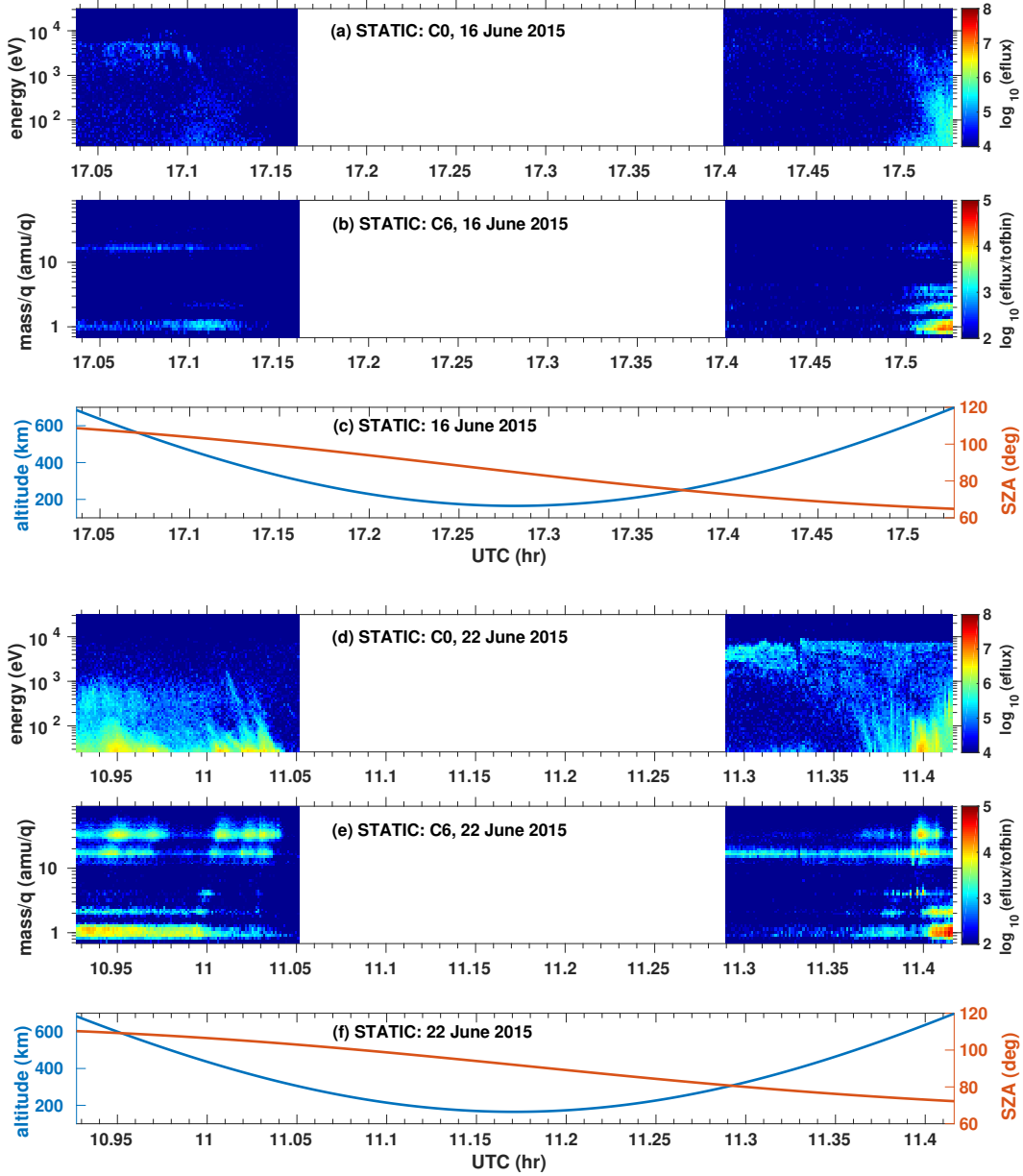


Figure 5. STATIC energy-time spectrogram of omnidirectional ion energy flux (C0 mode) during (a) orbit 1384/1385, and (d) orbit 1415/1416, STATIC mass-time spectrogram of omnidirectional ion energy flux (C6 mode) during (b) orbit 1384/1385, and (e) orbit 1415/1416 (c, f) altitude and SZA during the MAVEN orbit leg corresponding to the STATIC observations. The eflux is expressed in units of differential energy flux ($\text{eV}/[\text{eV cm}^2 \text{sr s}]$). The white gaps on (a, b, d, e) corresponds to altitudes below 300 km.

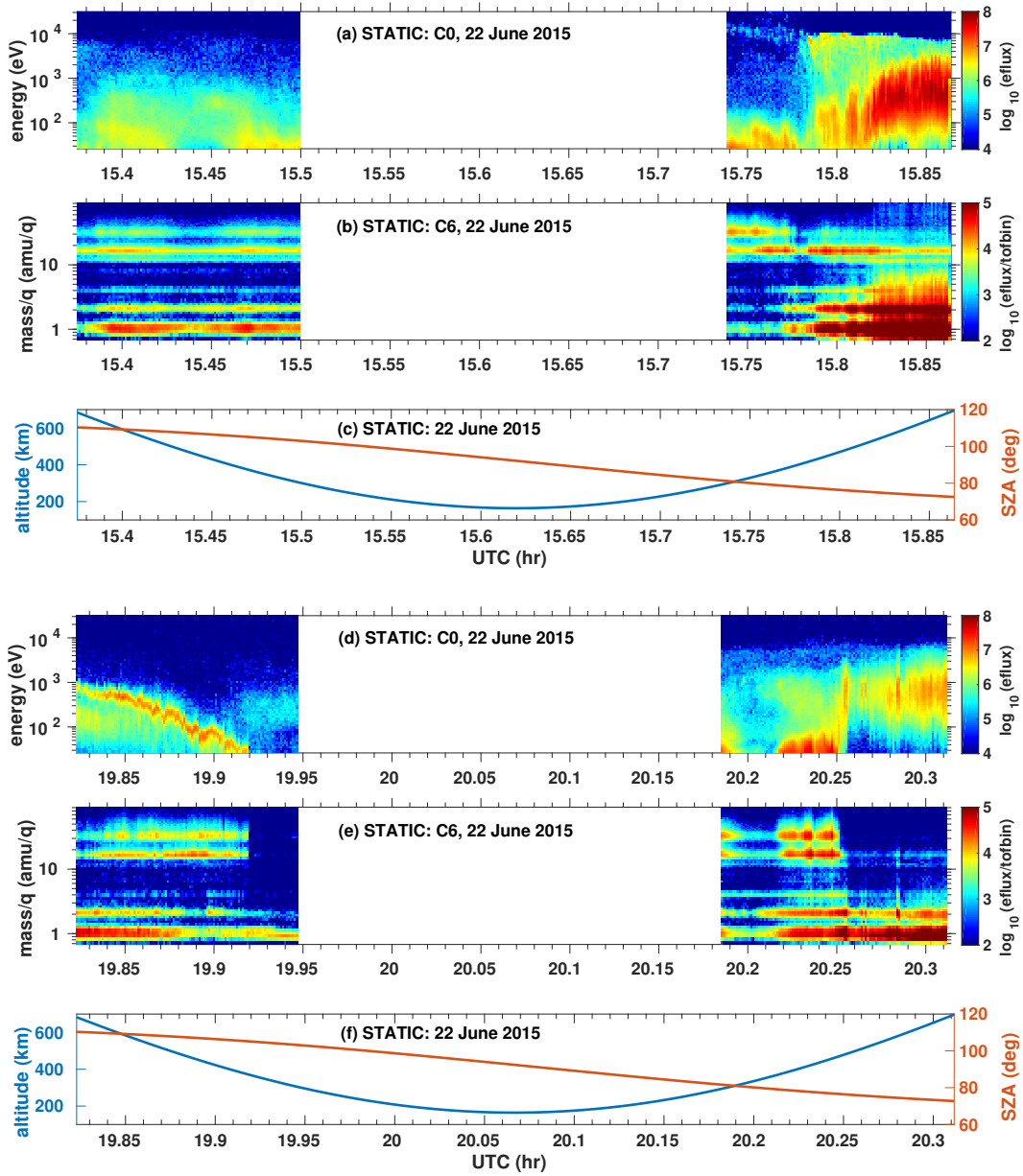


Figure 6. STATIC energy-time spectrogram of omnidirectional ion energy flux (C0 mode) during (a) orbit 1416/1417, and (d) orbit 1417/1418, STATIC mass-time spectrogram of omnidirectional ion energy flux (C6 mode) during (b) orbit 1416/1417, and (e) orbit 1417/1418 (c, f) altitude and SZA during the MAVEN orbit leg corresponding to the STATIC observations. The eflux is expressed in units of differential energy flux ($\text{eV}/[\text{eV cm}^2 \text{sr s}]$). The white gaps on (a, b, d, e) corresponds to altitudes below 300 km.

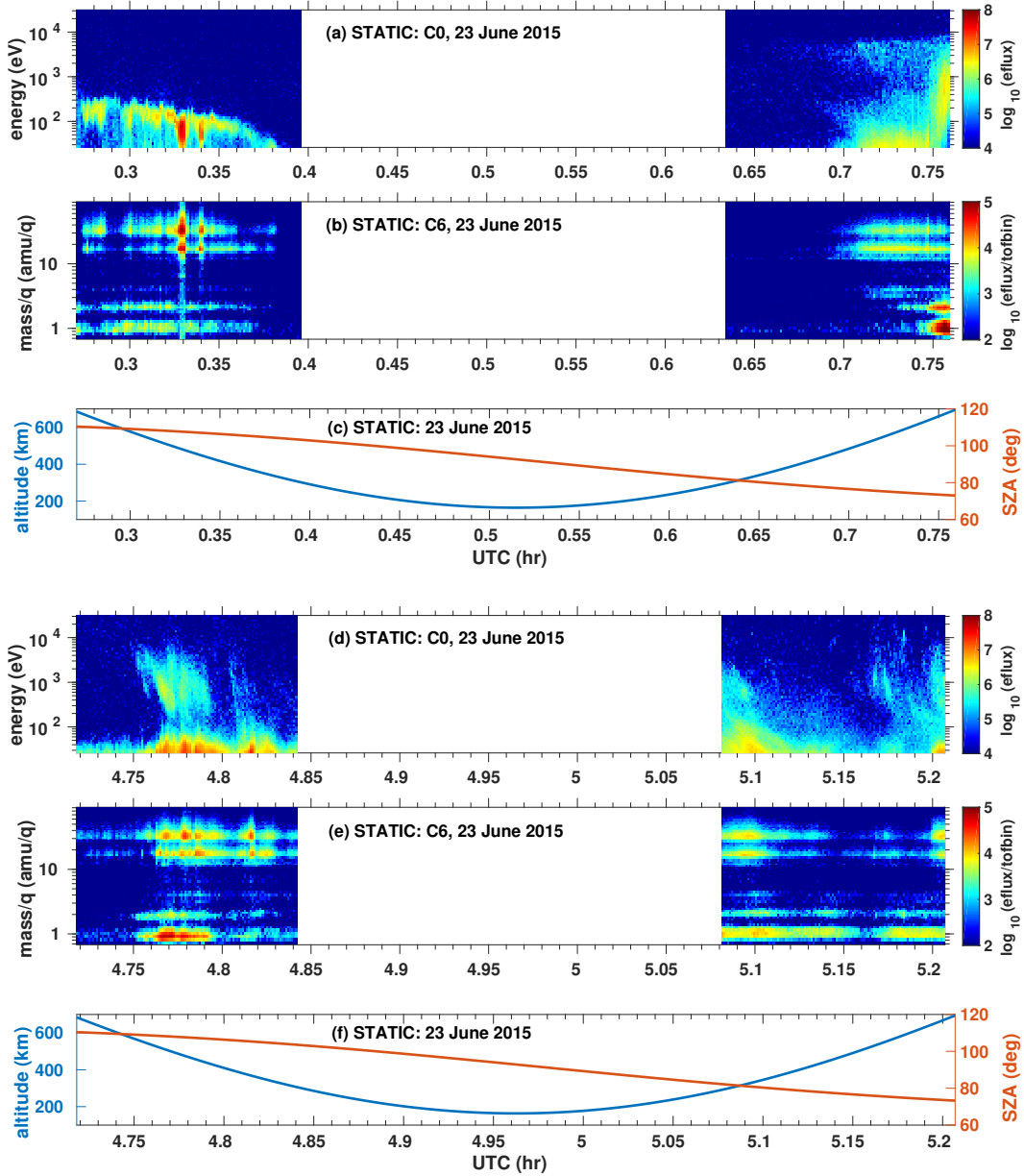


Figure 7. STATIC energy-time spectrogram of omnidirectional ion energy flux (C0 mode) during (a) orbit 1418/1419, and (d) orbit 1419/1420, STATIC mass-time spectrogram of omnidirectional ion energy flux (C6 mode) during (b) orbit 1418/1419, and (e) orbit 1419/1420 (c, f) altitude and SZA during the MAVEN orbit leg corresponding to the STATIC observations. The efflux is expressed in units of differential energy flux ($\text{eV}/[\text{eV cm}^2 \text{sr s}]$). The white gaps on (a, b, d, e) corresponds to altitudes below 300 km.

where the profiles returns to quiet time state (orbit 1420 shown in Figure 3a).

It may be noted that STATIC was operating at energies above 25 eV during the observation period shown in this paper. Hence, the detected ions represents the suprathermal tail of ram ions, which are tailward accelerated by the enhanced solar wind. The observations above 300 km only are shown, so that the spacecraft potential is minimal and can be assumed to be small (that is, about -2 V). It may also be noted that the ion energy flux in the STATIC mass spectrograms are divided with number of TOF bins in each mass bin, since the different TOF bins are summed in order to maintain a constant mass independent of energy (J. P. McFadden, personal communication).

The inbound orbits 1383, 1384 (quiet), 1416 and 1417 (disturbed), as well as outbound orbits 1384, 1385 (quiet), 1417 and 1418 (disturbed) passed through strong crustal field regions in the southern hemisphere. During quiet periods, the topside ionospheric profiles over the crustal field region were more or less identical to those measured outside the crustal field region. Therefore, the observed topside depletions during the disturbed period can be directly linked with the enhanced solar wind conditions, rather than the presence of crustal magnetic fields.

4 Discussion

The CIR shock accelerated a significant number of particles at 1.5 AU, which are detected as enhanced flux of SEP ions [Thampi *et al.*, 2019]. These enhanced energetic particles and CIR-associated magnetic field compressions could significantly affect the topside ionosphere of Mars, and the topology of Mars-solar wind interaction. The observed lower ionopause altitude (~ 400 km) during orbit 1417 is primarily due to the enhanced solar wind dynamic pressure, and the dayside ionosphere returns to the normal state in the declining speed region of the HSS, on the next orbit itself (Figure 3b). During orbit 1417 outbound, the electron density below 200 km is increased to $4 \times 10^4 \text{ cm}^{-3}$, which is around 200% increase in response to the topside day time compression, in comparison with quiet time mean. This is similar to the response during an interplanetary CME [Thampi *et al.*, 2018]. However, a striking feature in response to the CIR passage is that on the nightside, the topside ionosphere is significantly depleted for 5 consecutive orbits, from orbit 1415 to orbit 1419 (Figure 3a). The electron temperatures derived from the LPW indicate increased temperature (above 9000 K) only during orbit 1417 on the dayside (Figure 4b), while, on the nightside the observed increase in temperature is higher (above 12000 K) and persists for more than one orbit (Figure 4a).

This is similar to the observations reported by Cravens *et al.* [1982] on the Venusian nightside ionosphere that the depleted electron densities are accompanied by enhancement in electron temperatures along with large coherent horizontal magnetic fields. The solar wind dynamic pressures were observed to be larger than average conditions during the orbits when ionosphere is found to be depleted. The dayside ionopause was seen to be at a lower altitude when the solar wind dynamic pressure is large. Therefore, if the vertical extent of the dayside ionosphere is severely reduced, then the reservoir for the sustenance of nightside ionosphere can become smaller, and the supply of the ions would be curtailed [Cravens *et al.*, 1982]. In the present observations during CIR event, this is not the likely scenario for the extended depletion of topside ionosphere, because the dayside compression is observed only for a shorter duration. For the Venusian nightside ionosphere, Cravens *et al.* [1982] had suggested that the large coherent and horizontal magnetic field observed for depleted ionosphere might have (a) inhibited the downward diffusion, thus reducing the supply of ions to lower altitudes, and (b) inhibited the wake electron precipitation, thus shutting down a significant source for nightside ionization. In the case of Mars, these possi-

bilities are not likely because of two reasons: (1) at lower altitudes, the differences of night time electron density compared to the quiet time are not significant. In the case of Mars, the downward diffusion is not the major source for sustaining the nightside ionosphere [Fowler *et al.*, 2015]. Therefore, the extent of nightside ionosphere need not be linked directly to the dayside ionopause altitude, and this is in concurrence with the LPW observations. (2) If the electron precipitation were significantly curtailed, the ionosphere in the lower altitudes also might have depleted significantly [Fowler *et al.*, 2015], which is not the case in this event.

The Martian ionospheric ions are produced in the dayside and are picked up by the solar wind, accelerated and are swept away in the solar wind electric field direction. During CIRs, the mass loading of the solar wind plasma increases due to a deeper penetration of the interplanetary magnetic flux tubes into the ionosphere. The gyroradius of picked up O^+ ions before CIR passage (on 20 June 2015) is about ~ 30100 km (corresponding to the average solar wind velocity of 300 km sec^{-1} and magnetic field strength of 1.6 nT). After CIR passage (on 22 June 2015), the gyroradius of O^+ pickup ions is around ~ 8500 km (corresponding to the average solar wind velocity of 450 km sec^{-1} and magnetic field strength of 8.7 nT). The ratio of gyroradii after and before CIR shock is about 0.28 . The reduction in gyroradii of heavy ions may explain the enhanced STATIC ion energy fluxes at exospheric altitudes observed during the CIR. This may also explain the enhanced STATIC ion energy fluxes in the nightside close to the terminator above 300 km altitude.

These values of gyroradii are similar to those reported by Hara *et al.* [2011] inferred using MEX observations and ACE observations at ~ 1 AU. Hence the results indicate that when the strength of the IMF is enhanced due to the compressed IMF structure of the CIR, the gyroradii of the picked up planetary ions, such as O^+ becomes smaller (comparable to the Martian diameter) and therefore they can be found in the nightside ionosphere of Mars in the vicinity of ionospheric and exospheric altitudes. Using MEX data, Edberg *et al.* [2010] showed that the tailward flux of O^+ in the Martian ionosphere is significantly higher during CIR passage compared to quiet times. The photoionization of neutrals in the topside ionosphere produce ions which can be picked up by the sheath plasma and carried to the nightside [Cravens *et al.*, 1982]. This low density mass loaded ionosheath flow will also deplete the topside night time ionosphere. Our observations of enhanced heavy ion flux in the nightside sector corroborates with this (Figures 5-7). The present study also indicate that these enhanced energetic heavy ions can significantly deplete the topside ionosphere, as evident from the topside electron densities in the nightside observed by the LPW instrument. Therefore, the present observations suggest that the enhanced pickup and sputtering in the nightside during CIR event is the major cause for the depleted ionization on the topside night time ionosphere of Mars. The feature of occurrence of the heavy ion precipitation during CIR passage is different from the conventional expectation of constant ion precipitation. Hence the dynamic solar wind conditions indeed play a major role in the efficiency of pickup and sputtering processes and hence the atmospheric escape at Mars.

5 Summary and Conclusions

The response of ionosphere of Mars to the passage of CIR of June 2015 is studied using observations from MAVEN mission. The CIR arrival was observed at Mars by enhancements in solar wind density, velocity, and dynamic pressure, and increased and fluctuating IMF. The CIR event was accompanied by solar energetic particles (that is, energetic electrons and ions). The LPW instrument onboard MAVEN provides the electron density and electron temperature of the Martian ionosphere. We observe that the dayside ionosphere is significantly compressed during the peak of solar wind dynamic pressure enhancement (~ 14 nPa). This response is similar to the dayside ionospheric response to an interplanetary CME. But in contrast, we observe that the nightside electron density depletes for a longer period of time. The electron temperatures are also enhanced during the period of thermal plasma

depletion on the Martian nightside ionosphere. STATIC instrument onboard MAVEN observed enhanced fluxes of energetic protons and heavy ions (energies above 25 eV upto few keV) in the Martian exosphere during the impact of CIR. The planetary ions picked up by the solar wind are observed as enhanced flux of heavy ions in the vicinity of Mars at ionospheric altitudes. The gyroradius of O^+ pickup ions are observed to be relatively small during the ion precipitation. The observations indicate that the low density mass loaded tailward flow could be a major candidate for depleting the topside night time ionosphere.

Acknowledgments

The work is supported by the Indian Space Research Organisation (ISRO). The LPW electron density (Level 2, version 2, revision 2) and electron temperature data (Level 2, version 3, revision 2), STATIC ion energy flux data (Level 2, version 2, revision 0), SWIA solar wind ion data (Level 2, version 1, revision 1), SWEA solar wind electron data (Level 2, version 4, revision 1), MAG IMF data (Level 2, version 1, revision 2), and SEP solar wind energetic particle flux data (Level 2, Version 4, Revision 2) used in this work are taken from the Planetary Data System (<https://pds.nasa.gov/>). We gratefully acknowledge the MAVEN team for the data. We thank James P. McFadden, Space Sciences Laboratory, University of California, Berkeley for the helpful discussion on STATIC data. The WSA-ENLIL+Cone simulations are taken from <http://helioweather.net/>, <https://iswa.ccmc.gsfc.nasa.gov/>. C. Krishnaprasad acknowledges the financial assistance provided by ISRO through a research fellowship.

References

- Acuña, M. H., J. E. P. Connerney, P. Wasilewski, R. P. Lin, K. A. Anderson, C. W. Carlson, J. McFadden, D. W. Curtis, D. Mitchell, H. Rème, C. Mazelle, J. A. Sauvaud, C. d’Uston, A. Cros, J. L. Medale, S. J. Bauer, P. Cloutier, M. Mayhew, D. Winterhalter, and N. F. Ness (1998), Magnetic field and plasma observations at Mars: Initial results of the Mars Global Surveyor mission, *Science*, *279*(5357), 1676–1680, doi:10.1126/science.279.5357.1676.
- Acuña, M. H., J. E. P. Connerney, N. F. Ness, R. P. Lin, D. Mitchell, C. W. Carlson, J. McFadden, K. A. Anderson, H. Rème, C. Mazelle, D. Vignes, P. Wasilewski, and P. Cloutier (1999), Global distribution of crustal magnetization discovered by the Mars Global Surveyor MAG/ER experiment, *Science*, *284*(5415), 790–793, doi:10.1126/science.284.5415.790.
- Andersson, L., R. E. Ergun, G. T. Delory, A. Eriksson, J. Westfall, H. Reed, J. McCauly, D. Summers, and D. Meyers (2015), The Langmuir Probe and Waves (LPW) instrument for MAVEN, *Space Science Reviews*, *195*(1), 173–198, doi:10.1007/s11214-015-0194-3.
- Andrews, D. J., L. Andersson, G. T. Delory, R. E. Ergun, A. I. Eriksson, C. M. Fowler, T. McEnulty, M. W. Morooka, T. Weber, and B. M. Jakosky (2015), Ionospheric plasma density variations observed at Mars by MAVEN/LPW, *Geophysical Research Letters*, *42*(21), 8862–8869, doi:10.1002/2015GL065241.
- Arkani-Hamed, J., and D. Boutin (2004), Paleomagnetic poles of Mars: Revisited, *Journal of Geophysical Research: Planets*, *109*(E3), doi:10.1029/2003JE002229.
- Borovsky, J. E., and M. H. Denton (2006), Differences between CME-driven storms and CIR-driven storms, *Journal of Geophysical Research: Space Physics*, *111*(A7), doi:10.1029/2005JA011447.
- Carovillano, R. L., and G. L. Siscoe (1969), Corotating structure in the solar wind, *Solar Physics*, *8*(2), 401–414, doi:10.1007/BF00155388.
- Chaufray, J. Y., R. Modolo, F. Leblanc, G. Chanteur, R. E. Johnson, and J. G. Luhmann (2007), Mars solar wind interaction: Formation of the Martian corona and atmospheric loss to space, *Journal of Geophysical Research: Planets*, *112*(E9), doi:10.1029/2007JE002915.

- Connerney, J. E. P., M. H. Acuña, N. F. Ness, G. Kletetschka, D. L. Mitchell, R. P. Lin, and H. Reme (2005), Tectonic implications of Mars crustal magnetism, *Proceedings of the National Academy of Sciences*, *102*(42), 14,970–14,975, doi:10.1073/pnas.0507469102.
- Connerney, J. E. P., J. Espley, P. Lawton, S. Murphy, J. Odom, R. Oliverson, and D. Sheppard (2015), The MAVEN Magnetic Field investigation, *Space Science Reviews*, *195*(1), 257–291, doi:10.1007/s11214-015-0169-4.
- Cravens, T., L. Brace, H. Taylor, C. Russell, W. Knudsen, K. Miller, A. Barnes, J. Mihalov, F. Scarf, S. Quenon, and A. Nagy (1982), Disappearing ionospheres on the nightside of Venus, *Icarus*, *51*(2), 271 – 282, doi:https://doi.org/10.1016/0019-1035(82)90083-5.
- Curry, S. M., J. G. Luhmann, Y. J. Ma, C. F. Dong, D. Brain, F. Leblanc, R. Modolo, Y. Dong, J. McFadden, J. Halekas, J. Connerney, J. Espley, T. Hara, Y. Harada, C. Lee, X. Fang, and B. Jakosky (2015), Response of Mars O⁺ pickup ions to the 8 March 2015 ICME: Inferences from MAVEN data-based models, *Geophysical Research Letters*, *42*(21), 9095–9102, doi:10.1002/2015GL065304, 2015GL065304.
- Diéval, C., G. Stenberg, H. Nilsson, N. J. T. Edberg, and S. Barabash (2013), Reduced proton and alpha particle precipitations at Mars during solar wind pressure pulses: Mars Express results, *Journal of Geophysical Research: Space Physics*, *118*(6), 3421–3429, doi:10.1002/jgra.50375.
- Dong, C., S. W. Bougher, Y. Ma, G. Toth, Y. Lee, A. F. Nagy, V. Tenishev, D. J. Pawlowski, M. R. Combi, and D. Najib (2015), Solar wind interaction with the Martian upper atmosphere: Crustal field orientation, solar cycle, and seasonal variations, *Journal of Geophysical Research: Space Physics*, *120*(9), 7857–7872, doi:10.1002/2015JA020990.
- Dubinin, E., K. Sauer, K. Baumgrtel, and R. Lundin (1997), The Martian magnetosheath: Phobos-2 observations, *Advances in Space Research*, *20*(2), 149 – 153, doi:https://doi.org/10.1016/S0273-1177(97)00525-5, Planetary Ionospheres and Magnetospheres.
- Dubinin, E., M. Fraenz, J. Woch, F. Duru, D. Gurnett, R. Modolo, S. Barabash, and R. Lundin (2009), Ionospheric storms on Mars: Impact of the corotating interaction region, *Geophysical Research Letters*, *36*(1), doi:10.1029/2008GL036559.
- Duru, F., G. D. A., F. R. A., W. J. D., M. D. D., and H. G. G. (2009), Steep, transient density gradients in the Martian ionosphere similar to the ionopause at Venus, *Journal of Geophysical Research: Space Physics*, *114*(A12), doi:10.1029/2009JA014711.
- Edberg, N. J. T., H. Nilsson, A. O. Williams, M. Lester, S. E. Milan, S. W. H. Cowley, M. Fränz, S. Barabash, and Y. Futaana (2010), Pumping out the atmosphere of Mars through solar wind pressure pulses, *Geophysical Research Letters*, *37*(3), n/a–n/a, doi:10.1029/2009GL041814, 103107.
- Elliott, H. A., R. A. Frahm, J. R. Sharber, T. A. Howard, D. Odstril, H. J. Opgenoorth, D. Andrew, O. Witasse, and M. Frnz (2013), The influence of corotating interaction regions and high speed streams on electrons in the Martian magnetosheath and ionosphere, *AIP Conference Proceedings*, *1539*(1), 390–393, doi:10.1063/1.4811067.
- Ergun, R. E., M. M. W., A. L. A., F. C. M., D. G. T., A. D. J., E. A. I., M. T., and J. B. M. (2015), Dayside electron temperature and density profiles at Mars: First results from the MAVEN Langmuir Probe and Waves instrument, *Geophysical Research Letters*, *42*(21), 8846–8853, doi:10.1002/2015GL065280.
- Fowler, C. M., L. Andersson, R. E. Ergun, M. Morooka, G. Delory, D. J. Andrews, R. J. Lillis, T. McEnulty, T. D. Weber, T. M. Chamandy, A. I. Eriksson, D. L. Mitchell, C. Mazelle, and B. M. Jakosky (2015), The first in situ electron temperature and density measurements of the Martian nightside ionosphere, *Geophysical Research Letters*, *42*(21), 8854–8861, doi:10.1002/2015GL065267.
- Girazian, Z., P. R. Mahaffy, R. J. Lillis, M. Benna, M. Elrod, and B. M. Jakosky (2017), Nightside ionosphere of Mars: Composition, vertical structure, and variability, *Journal of Geophysical Research: Space Physics*, *122*(4), 4712–4725, doi:10.1002/2016JA023508.
- Gosling, J., and V. Pizzo (1999), Formation and evolution of corotating interaction regions and their three dimensional structure, *Space Science Reviews*, *89*(1), 21–52, doi:10.1023/A:1005291711900.

- Halekas, J. S., E. R. Taylor, G. Dalton, G. Johnson, D. W. Curtis, J. P. McFadden, D. L. Mitchell, R. P. Lin, and B. M. Jakosky (2015), The Solar Wind Ion Analyzer for MAVEN, *Space Science Reviews*, *195*(1), 125–151, doi:10.1007/s11214-013-0029-z.
- Halekas, J. S., S. Ruhunusiri, Y. Harada, G. Collinson, D. L. Mitchell, C. Mazelle, J. P. McFadden, J. E. P. Connerney, J. R. Espley, F. Eparvier, J. G. Luhmann, and B. M. Jakosky (2016), Structure, dynamics, and seasonal variability of the Mars-solar wind interaction: MAVEN Solar Wind Ion Analyzer in-flight performance and science results, *Journal of Geophysical Research: Space Physics*, *122*(1), 547–578, doi:10.1002/2016JA023167.
- Hara, T., K. Seki, Y. Futaana, M. Yamauchi, M. Yagi, Y. Matsumoto, M. Tokumaru, A. Fedorov, and S. Barabash (2011), Heavy-ion flux enhancement in the vicinity of the Martian ionosphere during CIR passage: Mars Express ASPERA-3 observations, *Journal of Geophysical Research: Space Physics*, *116*(A2), doi:10.1029/2010JA015778.
- Hara, T., J. G. Luhmann, F. Leblanc, S. M. Curry, K. Seki, D. A. Brain, J. S. Halekas, Y. Harada, J. P. McFadden, R. Livi, G. A. DiBraccio, J. E. P. Connerney, and B. M. Jakosky (2017), MAVEN observations on a hemispheric asymmetry of precipitating ions toward the Martian upper atmosphere according to the upstream solar wind electric field, *Journal of Geophysical Research: Space Physics*, *122*(1), 1083–1101, doi:10.1002/2016JA023348.
- Harada, Y., D. A. Gurnett, A. J. Kopf, J. S. Halekas, S. Ruhunusiri, C. O. Lee, T. Hara, J. Espley, G. A. DiBraccio, D. L. Mitchell, C. Mazelle, D. E. Larson, and B. M. Jakosky (2017), Dynamic response of the Martian ionosphere to an interplanetary shock: Mars Express and MAVEN observations, *Geophysical Research Letters*, *44*(18), 9116–9123, doi:10.1002/2017GL074897.
- Jakosky, B. M., et al. (2015), The Mars Atmosphere and Volatile Evolution (MAVEN) Mission, *Space Science Reviews*, *195*, 3–48, doi:10.1007/s11214-015-0139-x.
- Jakosky, B. M., et al. (2015), MAVEN observations of the response of Mars to an interplanetary coronal mass ejection, *Science*, *350*(6261), doi:10.1126/science.aad0210.
- Larson, D. E., R. J. Lillis, C. O. Lee, P. A. Dunn, K. Hatch, M. Robinson, D. Glaser, J. Chen, D. Curtis, C. Tiu, R. P. Lin, J. G. Luhmann, and B. M. Jakosky (2015), The MAVEN Solar Energetic Particle investigation, *Space Science Reviews*, *195*(1), 153–172, doi:10.1007/s11214-015-0218-z.
- Leblanc, F., R. Modolo, S. Curry, J. Luhmann, R. Lillis, J. Y. Chaufray, T. Hara, J. McFadden, J. Halekas, F. Eparvier, D. Larson, J. Connerney, and B. Jakosky (2015), Mars heavy ion precipitating flux as measured by Mars Atmosphere and Volatile Evolution, *Geophysical Research Letters*, *42*(21), 9135–9141, doi:10.1002/2015GL066170.
- Leblanc, F., A. Martinez, J. Y. Chaufray, R. Modolo, T. Hara, J. Luhmann, R. Lillis, S. Curry, J. McFadden, J. Halekas, and B. Jakosky (2018), On Mars’s atmospheric sputtering after MAVEN’s first Martian year of measurements, *Geophysical Research Letters*, *45*(10), 4685–4691, doi:10.1002/2018GL077199.
- Lee, C. O., T. Hara, J. S. Halekas, E. Thiemann, P. Chamberlin, F. Eparvier, R. J. Lillis, D. E. Larson, P. A. Dunn, J. R. Espley, J. Gruesbeck, S. M. Curry, J. G. Luhmann, and B. M. Jakosky (2017), MAVEN observations of the solar cycle 24 space weather conditions at Mars, *Journal of Geophysical Research: Space Physics*, *122*(3), 2768–2794, doi:10.1002/2016JA023495.
- Lillis, R. J., D. A. Brain, S. W. Bougher, F. Leblanc, J. G. Luhmann, B. M. Jakosky, R. Modolo, J. Fox, J. Deighan, X. Fang, Y. C. Wang, Y. Lee, C. Dong, Y. Ma, T. Cravens, L. Andersson, S. M. Curry, N. Schneider, M. Combi, I. Stewart, J. Clarke, J. Grebowsky, D. L. Mitchell, R. Yelle, A. F. Nagy, D. Baker, and R. P. Lin (2015), Characterizing atmospheric escape from Mars today and through time, with MAVEN, *Space Science Reviews*, *195*(1), 357–422, doi:10.1007/s11214-015-0165-8.
- Luhmann, J. G., C. F. Dong, Y. J. Ma, S. M. Curry, S. Xu, C. O. Lee, T. Hara, J. Halekas, Y. Li, J. R. Gruesbeck, J. Espley, D. A. Brain, C. T. Russell, and B. M. Jakosky (2017), Martian magnetic storms, *Journal of Geophysical Research: Space Physics*, pp. n/a–n/a, doi:10.1002/2016JA023513, 2016JA023513.

- Lundin, R., D. E. M., K. H., N. O., P. N., and B. S. W. (1991), On the momentum transfer of the solar wind to the Martian topside ionosphere, *Geophysical Research Letters*, *18*(6), 1059–1062, doi:10.1029/90GL02604.
- Ma, Y. J., X. Fang, A. F. Nagy, C. T. Russell, and G. Toth (2014), Martian ionospheric responses to dynamic pressure enhancements in the solar wind, *Journal of Geophysical Research: Space Physics*, *119*(2), 1272–1286, doi:10.1002/2013JA019402, 2013JA019402.
- Ma, Y. J., C. T. Russell, X. Fang, C. F. Dong, A. F. Nagy, G. Toth, J. S. Halekas, J. E. P. Connerney, J. R. Espley, P. R. Mahaffy, M. Benna, J. McFadden, D. L. Mitchell, L. Andersson, and B. M. Jakosky (2017), Variations of the Martian plasma environment during the ICME passage on 8 March 2015: A time-dependent MHD study, *Journal of Geophysical Research: Space Physics*, *122*(2), 1714–1730, doi:10.1002/2016JA023402, 2016JA023402.
- Martinez, A., F. Leblanc, J. Y. Chaufray, R. Modolo, N. Romanelli, S. Curry, J. Luhmann, R. Lillis, T. Hara, J. McFadden, J. Halekas, F. Eparvier, D. Larson, J. Connerney, Y. J. Ma, M. Holmström, O. Witasse, and B. Jakosky (2019), Variability of precipitating ion fluxes during the September 2017 event at Mars, *Journal of Geophysical Research: Space Physics*, *124*(1), 420–432, doi:10.1029/2018JA026123.
- Mays, M. L., A. Taktakishvili, A. Pulkkinen, P. J. MacNeice, L. Rastätter, D. Odstreil, L. K. Jian, I. G. Richardson, J. A. LaSota, Y. Zheng, and M. M. Kuznetsova (2015), Ensemble modeling of CMEs using the WSA–ENLIL+Cone model, *Solar Physics*, *290*(6), 1775–1814, doi:10.1007/s11207-015-0692-1.
- McFadden, J. P., O. Kortmann, D. Curtis, G. Dalton, G. Johnson, R. Abiad, R. Sterling, K. Hatch, P. Berg, C. Tiu, D. Gordon, S. Heavner, M. Robinson, M. Marckwardt, R. Lin, and B. Jakosky (2015), MAVEN Suprathermal and Thermal Ion Composition (STATIC) instrument, *Space Science Reviews*, *195*(1), 199–256, doi:10.1007/s11214-015-0175-6.
- Mitchell, D. L., C. Mazelle, J.-A. Sauvaud, J.-J. Thocaven, J. Rouzaud, A. Fedorov, P. Rouger, D. Toublanc, E. Taylor, D. Gordon, M. Robinson, S. Heavner, P. Turin, M. Diaz-Aguado, D. W. Curtis, R. P. Lin, and B. M. Jakosky (2016), The MAVEN Solar Wind Electron Analyzer, *Space Science Reviews*, *200*, 495–528, doi:10.1007/s11214-015-0232-1.
- Morgan, D. D., D. A. Gurnett, D. L. Kirchner, J. D. Winningham, R. A. Frahm, D. A. Brain, D. L. Mitchell, J. G. Luhmann, E. Nielsen, J. R. Espley, M. H. Acua, and J. J. Plaut (2010), Radar absorption due to a corotating interaction region encounter with Mars detected by MARSIS, *Icarus*, *206*(1), 95 – 103, doi:https://doi.org/10.1016/j.icarus.2009.03.008, solar Wind Interactions with Mars.
- Odstreil, D. (2003), Modeling 3-D solar wind structure, *Advances in Space Research*, *32*(4), 497 – 506, doi:https://doi.org/10.1016/S0273-1177(03)00332-6, Heliosphere at Solar Maximum.
- Opgenoorth, H. J., D. J. Andrews, M. Frnz, M. Lester, N. J. T. Edberg, D. Morgan, F. Duru, O. Witasse, and A. O. Williams (2013), Mars ionospheric response to solar wind variability, *Journal of Geophysical Research: Space Physics*, *118*(10), 6558–6587, doi:10.1002/jgra.50537.
- Parker, E. N. (1958), Dynamics of the Interplanetary Gas and Magnetic Fields, *The Astrophysical Journal*, *128*, 664, doi:10.1086/146579.
- Prise, A. J., L. K. Harra, S. A. Matthews, C. S. Arridge, and N. Achilleos (2015), Analysis of a coronal mass ejection and corotating interaction region as they travel from the Sun passing Venus, Earth, Mars, and Saturn, *Journal of Geophysical Research: Space Physics*, *120*(3), 1566–1588, doi:10.1002/2014JA020256.
- Russell, C. T. (1979), Planetary magnetism, *Reviews of Geophysics*, *17*(2), 295–301, doi:10.1029/RG017i002p00295.
- Sarabhai, V. (1963), Some consequences of nonuniformity of solar wind velocity, *Journal of Geophysical Research*, *68*(5), 1555–1557, doi:10.1029/JZ068i005p01555.
- Smith, E. J., and J. H. Wolfe (1976), Observations of interaction regions and corotating shocks between one and five AU: Pioneers 10 and 11, *Geophysical Research Letters*, *3*(3), 137–140, doi:10.1029/GL003i003p00137.

- Taylor, H. A., P. A. Cloutier, M. Dryer, S. T. Suess, A. Barnes, and R. S. Wolff (1985), Response of Earth and Venus ionospheres to corotating solar wind stream of 3 July 1979, *Earth, Moon, and Planets*, *32*(3), 275–290, doi:10.1007/BF00054217.
- Steckiewicz, M., C. Mazelle, P. Garnier, N. Andr, E. Penou, A. Beth, J.-A. Sauvaud, D. Toubanc, D. L. Mitchell, J. P. McFadden, J. G. Luhmann, R. J. Lillis, J. E. P. Connerney, J. R. Espley, L. Andersson, J. S. Halekas, D. E. Larson, and B. M. Jakosky (2015), Altitude dependence of nightside Martian suprathermal electron depletions as revealed by MAVEN observations, *Geophysical Research Letters*, *42*(21), 8877–8884, doi:10.1002/2015GL065257.
- Sánchez-Cano, B., B. E. S. Hall, M. Lester, M. L. Mays, O. Witasse, R. Ambrosi, D. Andrews, M. Cartacci, A. Cicchetti, M. Holmström, S. Imber, P. Kajdi, S. E. Milan, R. Noschese, D. Odstrčil, H. Opgenoorth, J. Plaut, R. Ramstad, and K. I. Reyes-Ayala (2017), Mars plasma system response to solar wind disturbances during solar minimum, *Journal of Geophysical Research: Space Physics*, *122*(6), 6611–6634, doi:10.1002/2016JA023587.
- Thampi, S. V., C. Krishnaprasad, A. Bhardwaj, Y. Lee, R. K. Choudhary, and T. K. Pant (2018), MAVEN observations of the response of Martian ionosphere to the interplanetary coronal mass ejections of March 2015, *Journal of Geophysical Research: Space Physics*, *123*(8), 6917–6929, doi:10.1029/2018JA025444.
- Thampi, S. V., C. Krishnaprasad, P. R. Shreedevi, T. K. Pant, and A. Bhardwaj (2019), Acceleration of energetic ions in corotating interaction region near 1.5 AU: Evidence from MAVEN, Submitted to *The Astrophysical Journal Letters*.
- Vogt, M. F., P. Withers, P. R. Mahaffy, M. Benna, M. K. Elrod, J. S. Halekas, J. E. P. Connerney, J. R. Espley, D. L. Mitchell, C. Mazelle, and B. M. Jakosky (2015), Ionopause-like density gradients in the Martian ionosphere: A first look with MAVEN, *Geophysical Research Letters*, *42*(21), 8885–8893, doi:10.1002/2015GL065269, 2015GL065269.
- Wang, Y., J. G. Luhmann, X. Fang, F. Leblanc, R. E. Johnson, Y. Ma, and W. Ip (2015), Statistical studies on Mars atmospheric sputtering by precipitating pickup O⁺: Preparation for the MAVEN mission, *Journal of Geophysical Research: Planets*, *120*(1), 34–50, doi:10.1002/2014JE004660.
- Wei, Y., M. Fraenz, E. Dubinin, J. Woch, H. Lhr, W. Wan, Q.-G. Zong, T. L. Zhang, Z. Y. Pu, S. Y. Fu, S. Barabash, R. Lundin, and I. Dandouras (2012), Enhanced atmospheric oxygen outflow on Earth and Mars driven by a corotating interaction region, *Journal of Geophysical Research: Space Physics*, *117*(A3), doi:10.1029/2011JA017340.
- Williams, A. O., N. J. T. Edberg, S. E. Milan, M. Lester, M. Frnz, and J. A. Davies (2011), Tracking corotating interaction regions from the Sun through to the orbit of Mars using ACE, MEX, VEX, and STEREO, *Journal of Geophysical Research: Space Physics*, *116*(A8), doi:10.1029/2010JA015719.